The Astrophysical Journal Letters, 868:L6 (9pp), 2018 November 20 https://doi.org/10.3847/2041-8213/aaedb2

Biosignature Anisotropy Modeled on Temperate Tidally Locked M-dwarf Planets

Howard Chen[1], Eric T. Wolf[2,3], Ravi Kopparapu[3,4], Shawn Domagal-Goldman[3,4], and Daniel E. Horton[1]
[1] Department of Earth and Planetary Sciences, Center for Interdisciplinary Exploration & Research in Astrophysics (CIERA), Northwestern University, Evanston, IL 60202, USA; howard@earth.northwestern.edu
[2] Laboratory for Atmospheric and Space Physics, Department of Atmospheric and Oceanic Sciences, University of Colorado Boulder, Boulder, CO 80309, USA
[3] NASA Astrobiology Institute Virtual Planetary Laboratory, Seattle, WA 98194, USA
[4] NASA Goddard Spaceflight Center, Greenbelt, MD 20771, USA
Received 2018 September 10; revised 2018 October 23; accepted 2018 October 29; published 2018 November 15

Abstract

A planet's atmospheric constituents (e.g., O_2, O_3, H_2O_v, CO_2, CH_4, and N_2O) can provide clues to its surface habitability, and may offer biosignature targets for remote life detection efforts. The plethora of rocky exoplanets found by recent transit surveys (e.g., the *Kepler* mission) indicates that potentially habitable systems orbiting K- and M-dwarf stars may have very different orbital and atmospheric characteristics than Earth. To assess the physical distribution and observational prospects of various biosignatures and habitability indicators, it is important to understand how they may change under different astrophysical and geophysical configurations, and to simulate these changes with models that include feedbacks between different subsystems of a planet's climate. Here we use a three-dimensional (3D) Chemistry–Climate model (CCM) to study the effects of changes in stellar spectral energy distribution (SED), stellar activity, and planetary rotation on Earth analogs and tidally locked planets. Our simulations show that, apart from shifts in stellar SEDs and UV radiation, changes in illumination geometry and rotation-induced circulation can influence the global distribution of atmospheric biosignatures. We find that the stratospheric day-to-nightside mixing ratio differences on tidally locked planets remain low (<20%) across the majority of the canonical biosignatures. Interestingly, however, secondary photosynthetic biosignatures (e.g., C_2H_6S) show much greater (∼67%) day-to-nightside differences, and point to regimes in which tidal locking could have observationally distinguishable effects on phase curve, transit, and secondary eclipse measurements. Overall, this work highlights the potential and promise for 3D CCMs to study the atmospheric properties and habitability of terrestrial worlds.

Key words: astrobiology – planets and satellites: atmospheres – planets and satellites: terrestrial planets – stars: low-mass

1. Introduction

A promising approach in the hunt for life beyond Earth is through the detection of biosignatures—biologically produced compounds such as O_2, O_3, CH_4, N_2O, and CO_2—in the atmospheres of terrestrial planets orbiting the putative habitable zones (HZs) of nearby stars (Lovelock 1975; Sagan et al. 1993; Seager et al. 2009; Kasting et al. 2015).

In recent years, the convergence of our ability to detect, confirm, and characterize extrasolar planets has profoundly strengthened the prospects of finding life on other worlds. Consistently improving measurements of stellar mass, radius, and distance allows more accurate constraints on their attending planets (Mann et al. 2015). Large-scale observational surveys such as the M-Earth project, TRAPPIST survey, Hungarian Automated Telescope Network, *Kepler* Space Telescope, and Transiting Exoplanet Satellite Survey have detected planets in the habitable zones around these stars (Thompson et al. 2018) and will continue to monitor closer and brighter systems for Earth-sized planets (Barclay et al. 2018). Simultaneously, follow-up characterization efforts of these confirmed planets were able to resolve atmospheres of much smaller planets than past efforts (e.g., HAT-P-26b; Wakeford et al. 2017). Looking ahead, a variety of instruments are being designed with life detection goals in mind. This includes ground-based observatories such as the European Extremely Large Telescope (E-ELT), Giant Magellen Telescope (GMT), and Thirty-Meter Telescope (TMT), as well as space-based missions such as the *James Webb Space Telescope* (*JWST*), Large UV/Optical/IR Surveyor (LUVOIR), Origins Space Telescope, and Habitable Exoplanet Imaging Observatory (HabEx). HabEx and LUVOIR in particular would enable characterization of potentially habitable Earth-sized rocky planets in our solar neighborhood (≲100 pc; Bolcar et al. 2016; Mennesson et al. 2016; Batalha et al. 2018).

The recent discoveries of Proxima Centauri b (Anglada-Escudé et al. 2016) and the TRAPPIST-1 system (Gillon et al. 2017) demonstrate that analyses of small rocky planets are within reach. However, many of these planets orbit extremely close to their host M-type stars (0.02–0.2 au) and are susceptible to trapping by tidal-forces (Tarter et al. 2007). Tidally locked but potentially habitable planets are expected to be common in HZs of low-mass stars (∼15%; Dressing & Charbonneau 2015)—which dominate our solar neighborhood stellar population (∼70%; Henry et al. 2006). Concurrently, our earliest opportunity for a biosignature search will likely come from the *JWST* and ground-based extremely large telescopes (E-ELT, GMT, and TMT); these observatories will enable spectroscopic observations of rocky planets around K- and M-type stars. It is therefore likely that our first opportunity to measure atmospheres of rocky worlds will be tidally locked terrestrial planets around K- or M-dwarf stars.

Characterization of exoplanets primarily involves measuring starlight and terrestrial thermal emissions absorbed by planetary atmospheres as a function of wavelength. For transit spectroscopy, which will be the main tool for obtaining spectra from planets around M-dwarf stars, observations are biased toward atmospheric constituents across the terminators.

Therefore, interpreting spectroscopic observations requires inferring both the concentration and distribution of detectable gases. Such properties can be predicted by 3D global climate and chemistry–climate models (GCMs and CCMs). GCMs and CCMs are numerical models that employ laws of physics, fluid motion, and in the case of CCMs, chemistry to simulate movements, interactions, and climatic implications of a planet's atmospheric constituents and boundary conditions.

Previous simulations of atmospheres of tidally locked planets performed with 3D GCMs have demonstrated that habitable states of tidally locked planets are strong functions of (i) Coriolis force (Kopparapu et al. 2016; Way et al. 2016; Yang et al. 2016), (ii) stellar energy distribution (SED) and bolometric stellar flux (Kopparapu et al. 2017; Wolf 2017), (iii) atmospheric mass (Wordsworth 2015), and (iv) radiative transfer scheme (Yang et al. 2016). Despite the ability of GCMs to simulate key climatological factors, as demonstrated by these studies, their foci have primarily been on questions of habitability, rather than the concentrations and distributions of biologically produced gases and habitability indicators.

To study effects of tidal locking on atmospheric chemistry and molecular spectroscopic signals, models capable of resolving chemical speciation, reactions, and transport are needed. To date, exoplanet atmospheric photochemical predictions have largely relied on one-dimensional global-mean photochemistry-climate models (e.g., Kasting et al. 1984; Segura et al. 2005; Meadows et al. 2018a). These 1D models have been used to simulate synthetic spectra of hypothetical rocky planets under the influence of different host SEDs (Rauer et al. 2011; Rugheimer et al. 2015). However, 1D models employ relatively simple eddy-diffusion parameterizations for vertical transport and do not account for atmospheric dynamics, climate heterogeneities, or 3D geometric effects critical to observations. These factors are important as advection and diffusion can affect concentration, distribution, and ultimately the composition of an atmosphere (Seinfeld & Pandis 2012). In addition to altering photochemistry, as shown by 1D models, shifts in stellar SED can influence atmospheric circulation and climate (e.g., Shields et al. 2014; Fujii et al. 2017). Atmospheric chemistry and dynamics are thus interactive, and should ideally be simulated using fully coupled 3D model components.

Here, to better understand the observational potential of tidally locked planets, the integrated effects of atmospheric chemistry, photochemistry, and circulation are considered over the 3D geometry of a planet's atmosphere. In this Letter, we simulate Earth analogs and tidally locked planets around M-dwarf stars using a 3D CCM, while seeking to (i) elucidate the photochemical nature of Earth-like worlds, (ii) demonstrate the utility of 3D CCMs in terrestrial exoplanet studies, (iii) and advance model comparison efforts between 3D and 1D research communities.

2. Model Description and Experimental Setup

In this study, we employ the Community Atmosphere Model with Chemistry (CAM-chem), a subset of the National Center for Atmospheric Research (NCAR) Community Earth System Model (CESM v.1.2), to investigate atmospheres of Earth-like planets. CAM-chem is a 3D global CCM that simulates interactions of atmospheric chemistry, radiation, thermodynamics, and dynamics (for a complete model description, see Lamarque et al. 2012). CAM-chem combines the CAM4 atmospheric component with the fully implemented Model for Ozone and Related Chemical Tracers (MOZART) chemical transport model. CAM-chem resolves 97 gas phase species and aerosols linked by 196 chemical and photolytic reactions. CAM, the atmosphere component of the model, has seen wide applications in problems of paleoclimate and exoplanets (e.g., Wolf & Toon 2015; Kopparapu et al. 2016), whereas CAM-chem has largely been limited to studies of present Earth. All simulations presented were run for 30 Earth years and reported results are averaged over the last 20.

We simulate Earth analogs and tidally locked planets and assess the sensitivity of atmospheric biosignatures to three primary variables: (i) stellar spectral energy distribution, (ii) stellar UV radiation, and (iii) planetary rotation period. To simulate Earth analogs, we use a preindustrial Earth setup forced by solar spectral irradiance data (Lean et al. 1995), i.e., apart from the orbital parameters described below, our Earth-analog simulation uses identical boundary and initial conditions to Earth in 1850, prior to anthropogenic influences (Taylor et al. 2012). These conditions include atmospheric gases N_2 (78% by volume), O_2 (21%), and CO_2 (2.85×10^{-2}%) (MacFarling Meure et al. 2006). In addition, the model simulates the free-running evolution of H_2O_v and O_3, while CH_4 and N_2O surface fluxes are latitudinally variable (global mean CH_4: 7.23×10^{-7} and N_2O: 2.73×10^{-7} mol mol^{-1}). Throughout the remainder of the paper, we refer to this Earth–Sun simulation as the baseline.

We also modify CAM-chem to simulate tidally locked planets with initially Earth-like atmospheric compositions forced by M-dwarf SEDs. This SED was obtained from an open-source data set of an M6V star, Proxima Centauri, compiled by NASA's Virtual Planetary Laboratory (VPL) team and is available at http://vpl.astro.washington.edu/spectra/stellar/. We explore two SED-types (active and quiescent) that bracket the endmember ranges of stellar activity. VPL Proxima Cen. data is assumed to be moderately to highly active. To construct a quiescent M-dwarf SED, we swap out UV bands ($\lambda < 500$ nm) of the original Proxima Cen. data with that of a low-activity star (HD114710). For all exo-Earth simulations, we assume tidal locking (i.e., trapped in 1:1 spin-orbit resonances), with orbital periods of 50 Earth days. While we do not use self-consistent stellar-flux orbital period relationships (e.g., Kopparapu et al. 2016; Haqq-Misra et al. 2018), the idealized case studied here highlights the value of using CCMs for modeling chemical processes on slowly and synchronously rotating planets.

For both Earth and tidally locked exoplanet simulations, we set orbital parameters (obliquity, eccentricity, and precession) to zero, such that top-of-atmosphere incident stellar flux is symmetric about the equator. Incident bolometric stellar flux for all simulations is set to 1360 W m^{-2}. The substellar point for all simulations is fixed at (Earth's) latitude $= 0°$ and longitude $= 180°$, in the Pacific Ocean. Note that other studies (e.g., Lewis et al. 2018) have shown that surface type beneath a substellar point can modify water vapor availability, influencing water vapor-induced greenhouse and cloud radiative effects, and possibly atmospheric chemistry.

In all simulations, we assume present Earth's continental configuration, topography, mass, and radius. We use prognostic atmospheric and oceanic components of CESM, as well as prescribed preindustrial land, surface ice, and sea ice components. Horizontal resolution (latitude × longitude) is

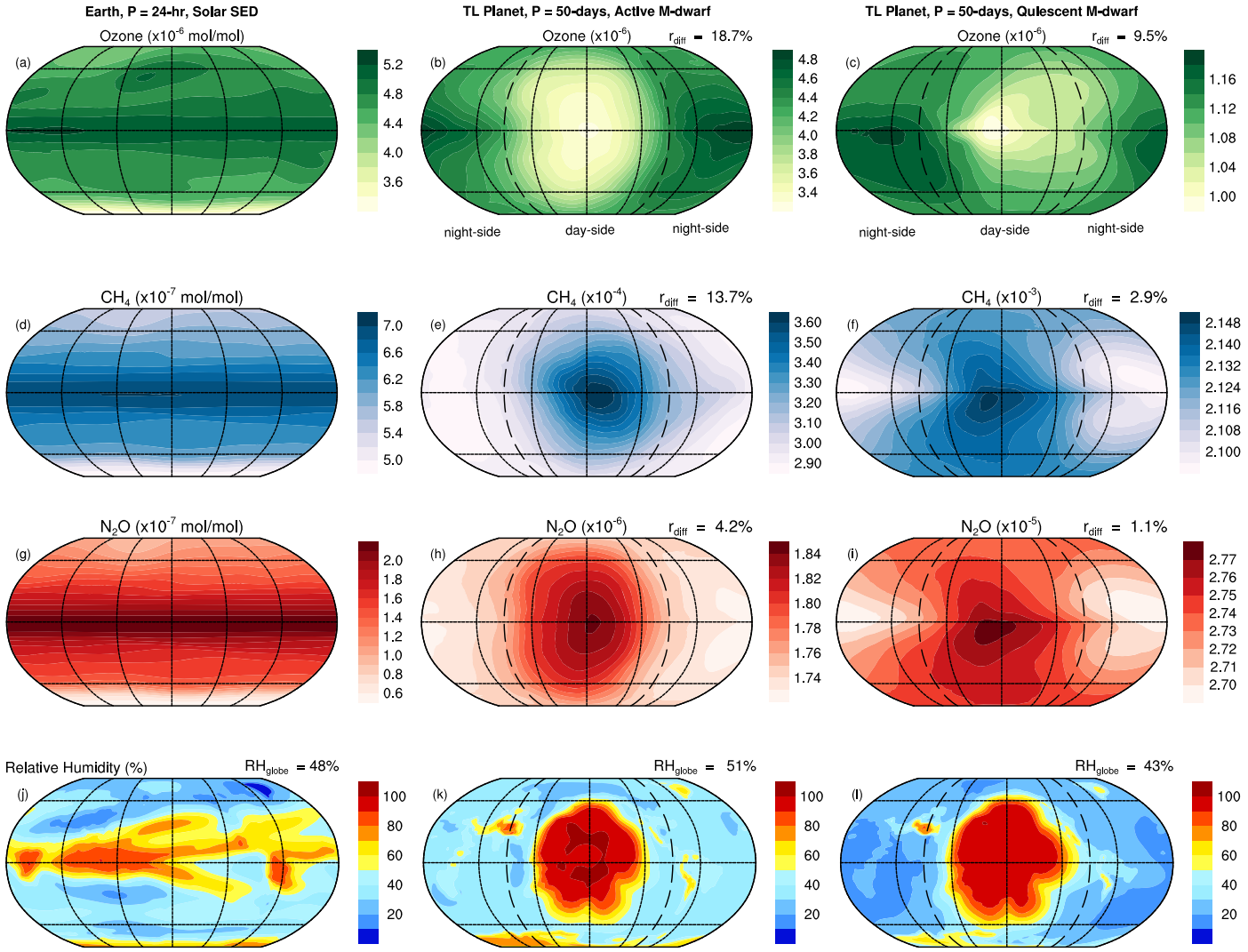

Figure 1. Global distribution of O_3, CH_4, and N_2O mixing ratios and relative humidity for Earth-like nontidally locked ($P = 24$ hr) Solar SED simulations ((a), (d), (g), (j)) and tidally locked ($P = 50$ days) active ((b), (e), (h), (k)) and quiescent ((c), (f), (i), (l)) M-dwarf SED simulations. Evidence of circulation- and photochemical-induced biosignature anisotropy are apparent. Day-to-nightside mixing ratio contrasts (r_{diff}) for tidally locked simulations are reported, while relative humidity is averaged across the globe (RH_{globe}). Gas mixing ratios are pressure-weighted vertical averages over the top of the model atmosphere (1-to-100 mb). Relative humidity is reported for the 200 mb pressure surface. Note differences in scaling factors used among experiments and constituents. Dashed-lines indicate locations of terminators.

set to $1.9° \times 2.5°$ with 26 vertical atmospheric levels and model top of 1 mb (~50 km). The land model is Community Land Model version 4.0 with noninteractive surface features. The ocean component is a thermodynamic slab model with prescribed heat flux values sourced from dynamical ocean simulations (e.g., Danabasoglu & Gent 2009).

Consistent with 1D studies (e.g., Segura et al. 2005; Rugheimer et al. 2015) and in alignment with our lack of terrestrial exoplanet observations, we assume atmospheric compositions, biological production, and dry deposition rates of gaseous species the same as those of preindustrial Earth. Apart from CH_4 and N_2O, global surface gas flux inputs are based on spatially explicit preindustrial monthly averages (e.g., DMS; Kettle & Andreae 2000). Due to SED sensitivities, CH_4 and N_2O surface flux boundary conditions are estimated via ancillary CCM simulations that allow for the emergence of stellar SED-dependent flux magnitudes (i.e., WACCM; Neale et al. 2010). Emergent SED-consistent N_2O and CH_4 flux estimates are temporally and spatially fixed in active and quiescent M-dwarf simulations at CH_4: 3.5×10^{-4} and 2.3×10^{-3} mol mol^{-1} and N_2O: 2.5×10^{-6} and 3.2×10^{-5} mol mol^{-1}, respectively. Given uncertainties inherent in flux estimates, sensitivity experiment and day-to-nightside mixing ratio comparisons should focus on relative rather than absolute differences.

3. Results

Three general observations can be made from our simulated 3D global distributions of O_3, CH_4, N_2O, and DMS on Earth-like and tidally locked planets (Figures 1 and 4): (i) Changes in mixing ratios of O_3, CH_4, and N_2O are primarily due to different levels of stellar UV flux among the three SED data sets. (ii) Introduction of tidal locking modifies globally homogeneous gas distributions that characterize Earth-like scenarios. (iii) Heterogeneous surface to atmosphere flux distributions (e.g., DMS) can influence the resultant mixing ratios of atmospheric constituents.

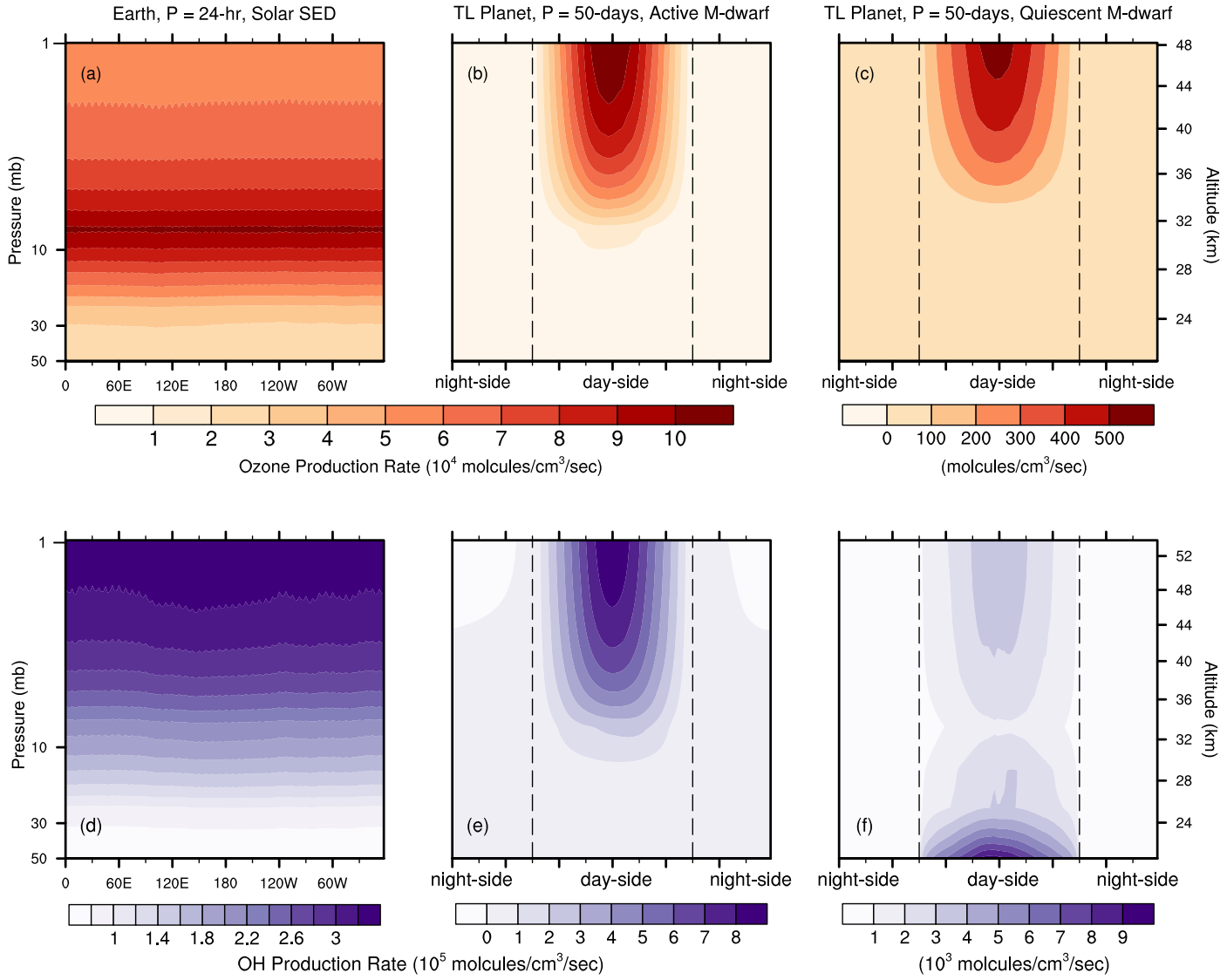

Figure 2. Stratospheric O_3 and OH production rates as functions of longitude for Earth-like nontidally locked ($P = 24$ hr) Solar SED simulations ((a), (d)) and tidally locked ($P = 50$ days) M-dwarf SED ((b), (c), (e), (f)) simulations. Photolytic processes drive ozone and hydroxyl radical production and help to explain many of the observed biosignature gas distributions in Figure 1. Note the vertical axis begins at 50 mb (20 km). Dashed-lines indicate locations of terminators.

To facilitate analysis of our results, we define a day-to-nightside mixing (mole) ratio contrast as:

$$r_{\rm diff} = \frac{r_{\rm day} - r_{\rm night}}{r_{\rm globe}}, \quad (1)$$

i.e., the relative difference between the two hemispheres, where $r_{\rm day}$ is the dayside hemispheric mixing ratio mean, $r_{\rm night}$ is the nightside mean, and $r_{\rm globe}$ is the global mean. The degree of anisotropy is loosely encapsulated in this parameter, which is analogous to the definition used by Koll & Abbot (2016) in the context of temperature contrasts. Values of $r_{\rm diff}$ for each respective experiment are shown in Figures 1 and 4 and will be discussed throughout the paper.

3.1. Ozone Distributions, Water Vapor Mixing Ratios, and Temperature Profiles

Ozone production and destruction depend on stellar UV activity, availability of molecular and atomic oxygen, and ambient meteorological conditions (P, T). As our simulated M-dwarf SED is moderately active in the UV bands, our results show similar quantities of ozone between the baseline Earth–Sun and tidally locked cases (Figures 1(a)–(c)). However, the quiescent SED, produces lower ozone concentrations above the tropopause (Figure 3(c)). These differences reflect specific stellar activity inputs. Quiescent M-dwarfs emit lower UV in the range responsible for ozone production ($160 < \lambda < 24$ nm). Moreover, calculated day-to-nightside mixing ratio differences $r_{\rm diff}$ are higher ($\sim$19%) in the active M-dwarf SED scenario.

Modulations to ozone concentration have major influences on distributions of other biosignature gases. This is due to substellar hemispheric production of excited state atomic oxygen $O(^1D)$ and constituent families of HO_x. Both $O(^1D)$ and HO_x constituents are reactive radicals important for atmospheric biogenic organo-compounds and hydrocarbons (e.g., CH_4, CH_3, HCL, and H_2S).

As ozone is photochemically produced, horizontal advection carries a portion to the nightside as evidenced by its presence in both hemispheres. The lifetime of ozone ($\sim$15 days), in

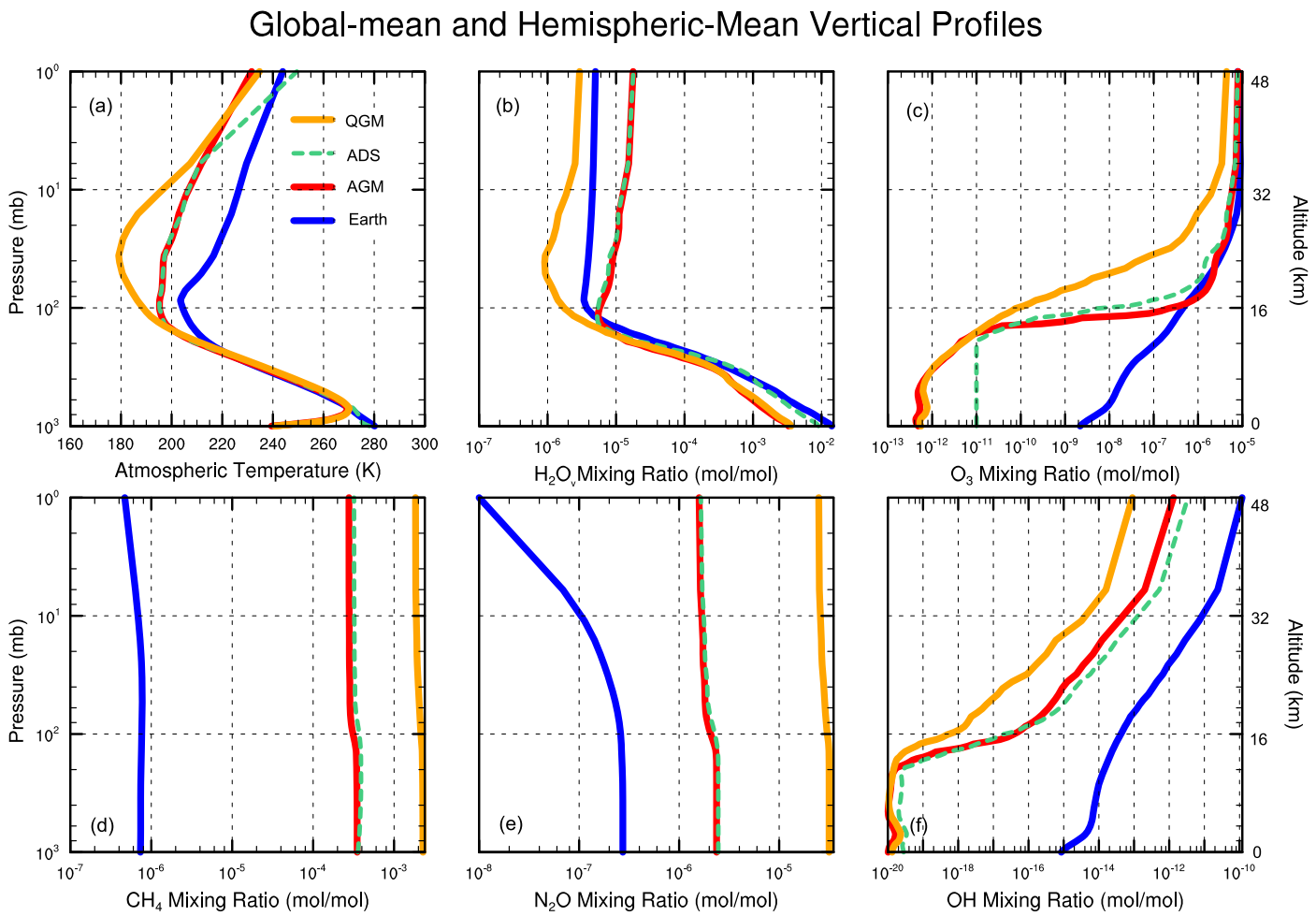

Figure 3. Vertical profiles of global-mean temperature (a) and mixing ratios of various gas phase species ((b), (c), (d), (e), and (f)). QGM (quiescent global mean) denotes global-mean values from simulations forced by a quiescent M-dwarf SED, AGM (active global mean) denotes those forced by an active M-dwarf SED, and ADS (active dayside) denotes dayside-mean values from simulations forced by an active M-dwarf SED. Note that axes are log-scaled and begin at planetary surfaces (∼1000 mb).

conjunction with day-to-nightside transport, is sufficient enough to sustain some nightside O_3, but not efficient enough to fully mix the atmosphere, allowing day-to-nightside contrast (∼19%; Figure 1(b)). Conversely, the product $O(^1D)$ shows limited transport effects due to a short lifetime (<5 s), reflected in its large r_{diff} value (∼300%; not shown). $O(^1D)$ is rapidly removed by either the R1 or R2 reaction pathway (Jacob 1999):

$$O(^1D) + H_2O_v \rightarrow 2OH \quad \text{(R1)}$$

$$O(^1D) + M(N_2,\ O_2) \rightarrow O(^3P) + M \quad \text{(R2)}$$

$$O(^3P) + O_2 + M \rightarrow O_3 + M. \quad \text{(R3)}$$

The higher ozone mixing ratios on tidally locked nightsides is explained by these reaction pathways (Figures 1(b)–(c)). Reaction R1, which creates the hydroxyl radical OH, predominantly occurs on the dayside due to the abundance of H_2O_v (Figures 2(e)–(f)). In R2, singlet oxygen returns to the triplet ground state, which can then recombine with oxygen to form ozone via R3. Considered together, significant dayside UV ozone destruction and enhanced removal of $O(^1D)$ by water vapor offset higher ozone production rates (Figure 3(b)), which helps to explain lower dayside ozone mixing ratios (Figure 1(b)–(c)).

Interaction of stellar UV photons with O_2 and O_3 can also be seen in vertical temperature profiles. On Earth-like planets, stratospheric temperature is primarily a function of incident UV flux ($200 < \lambda < 310$ nm) due to the role of O_3 absorption of shortwave photons. In our simulations, this feature is apparent in global and hemispherically averaged profiles. Our simulations indicate that upper-stratospheric temperatures increase (and inversions weaken) as UV radiation levels increase; from quiescent SED, to active SED, to the baseline Earth simulation (Figure 3(a)). Enhanced UV absorption by O_3 and O_2 increase temperatures above the tropopause, reducing the vertical gradient and inversion strength.

We now turn to discussing testability of our 3D model predictions. Based on simulated ozone distributions, the calculated r_{diff} (∼20%) is notable but unlikely to be discernible with current observational capabilities (Burrows 2014). However, this task may prove viable using future instruments (e.g., Greene et al. 2016). Proedrou & Hocke (2016) reached a similar conclusion by comparing total column ozone of a tidally locked Solar-SED Earth and found an ∼23% difference between mean ozone columns during four arbitrary phases due to varying viewing angles.

Compared with 1D model studies, our 3D simulations produce similar ozone mixing ratios (Table 1). However, we find substantially different Bond albedos, temperature, and water mixing ratio profiles. As a consequence of increased

Table 1
Model Comparisons of Approximate Global-mean Mixing Ratios of Various Gases

Study	Rauer et al. (2011)	Rugheimer et al. (2015)	This Work
Model	1D photochemical	EXO-P	NCAR's CAM-chem
SED data	AD Leonis[a]	Active M6 stellar model[b]	Proxima Cen.[c]
Bond albedo	N/A[d]	0.07	0.46
T_{surf} (K)	298	300	242
$O_{3,surf}$ (mol/mol)	8×10^{-11}	10^{-9}	9.4×10^{-13}
$CH_{4,surf}$ (mol/mol)	10^{-4}	1×10^{-3}	3.4×10^{-4}
N_2O_{surf} (mol/mol)	2.0×10^{-6}	1.7×10^{-6}	2.4×10^{-6}
H_2O_vsurf (mol/mol)	7.0×10^{-2}	5.0×10^{-2}	3.5×10^{-4}
$T^e_{100\ mb}$ (K)	251	245	200
$O_{3,100\ mb}$ (mol/mol)	10^{-8}	10^{-6}	5.2×10^{-7}
$CH_{4,100\ mb}$ (mol/mol)	10^{-6}	1×10^{-3}	3.1×10^{-4}
N_2O_{100mb} (mol/mol)	10^{-5}	5×10^{-7}	2.0×10^{-6}
H_2O_v100 mb (mol/mol)	10^{-7}	7.0×10^{-4}	5.8×10^{-6}

Notes. Approximate atmospheric temperature (units of kelvin) and mixing ratios of various gas phase species (units of mol/mol) simulated on Earth-like planets by various authors. All data reported are taken from simulations forced by active stellar SEDs that range from M6V to M8V dwarf stars.
[a] Active M3.5 eV star, $T_{\rm eff} = 3300$ K, $M = 0.41 M_{\odot}$.
[b] Part of a suite of stellar SED model data generated by Rugheimer et al. (2015) to represent the most active M-dwarf observations (e.g., PHOENIX or MUSCLES database).
[c] SED data from Virtual Planetary Laboratory's stellar spectrum database (Meadows et al. 2018a).
[d] Data not provided.
[e] Values reported at 100 mb.

dayside water vapor-induced opacity and substellar clouds on tidally locked planets, global-mean surface temperatures of both tidally locked simulations are ~40 K colder than the baseline (Figure 3(a)), while Bond albedos are substantially higher (Table 1), in agreement with GCM studies (Yang et al. 2013; Kopparapu et al. 2016, 2017). Colder global (and nightside) temperatures produce lower global water vapor mixing ratios than predicted by 1D models with clear-sky assumptions (i.e., pure water vapor without clouds). Conversely, dayside H_2O_v mixing ratios are greater due to humid updrafts at the substellar point (Figures 1(j)–(l)). Curiously, the quiescent M-dwarf SED simulation (Figure 1(l)) has lower global-mean relative humidity than the Earth-analog (Figure 1(j)) and the active M-dwarf case (Figure 1(k)). This is due to increased ozone mixing ratios and degree of UV absorption, which limit the photolysis of H_2O_v, in the more active SED simulations. Hence counterintuitively, more dayside H_2O_v destruction is experienced by the simulation under lower UV radiation. Such behaviors exemplify the value of CCM simulations, in which capturing feedbacks between 3D dynamical processes, solar forcing, and atmospheric chemistry is critical.

3.2. Types I and II Biosignatures: 3D CH_4 and N_2O Abundances

CH_4 and N_2O are important biosignatures produced by a myriad of bacterial metabolic pathways (Des Marais et al. 2002; Schwieterman et al. 2018). In Figures 1(d)–(f), we show modeled CH_4 distributions. High CH_4 mixing ratios for planets orbiting quiet M-dwarfs were first noted by Segura et al. (2005) using a 1D model, due to less OH in M-dwarf planet atmospheres:

$$CH_4 + OH \rightarrow CH_3 + H_2O. \quad \text{(R4)}$$

In our 3D CCM, we find similar global mean CH_4 increases in tidally locked simulations (Figures 1(e)–(f)). However, active and quiescent simulations have low CH_4 $r_{\rm diff}$ values (13.7% and 2.9%, respectively). Low $r_{\rm diff}$ values are explained by a mixture of competing processes. First, upwelling in tidally locked simulations occurs exclusively below the substellar point, as evidenced by upper-tropospheric moisture patterns (Figures 1(j)–(l)). Compared to the baseline, tidally locked meridional overturning circulation is strengthened, which brings greater moisture aloft. This, in conjunction with the dayside abundance of OH, removes CH_4 via R4. Increased dayside OH production (Figures 2(e)–(f)) is a consequence of abundant $O(^1D)$ and H_2O_v (R1), both of which are sparse on the nightside. These processes combine to limit dayside CH_4 and produce lower $r_{\rm diff}$ values than expected.

N_2O is primarily destroyed by UV photons ($\lambda < 220$ nm) and photooxidation by reactions with stratospheric $O(^1D)$ (Figure 1(g)–(i)). Hence predicted N_2O concentrations around active M-dwarfs are lesser than those with quiescent SEDs. For both active and quiescent SED simulations, higher concentrations within the substellar hemisphere are found (Figures 1(h)-(i)), similar to CH_4 behavior.

Interestingly, simulations forced by the active SED have greater stratospheric $r_{\rm diff}$ (CH_4: 13.7% and N_2O: 6.9%; Figures 1(e)–(h)) than those forced by quiescent SEDs (CH_4:

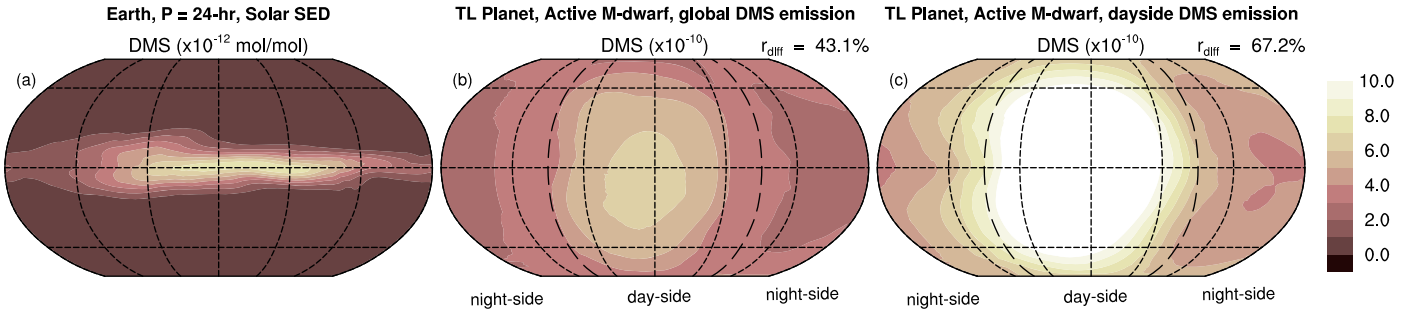

Figure 4. Global distribution of photosynthetic biosignature dimethyl sulfide (DMS, $(CH_3)_2S$) for Earth-like nontidally locked ($P = 24$ hr) Solar SED simulations (a), tidally locked ($P = 50$ days) active M-dwarf SED simulations with a global DMS flux assumption (b), and tidally locked with a dayside DMS flux assumption (c). Day-to-nightside mixing ratio differences (r_{diff}) for the tidally locked simulations are reported. Phototrophs are assumed to be only present on the permanently lit dayside in panel (c), which results in an enhanced stratospheric day-to-nightside mixing ratio contrast. Dashed-lines indicate locations of terminators.

2.9% and N_2O: 1.1%; Figures 1(f)–(i)). Higher r_{diff} values for active SED cases is somewhat counterintuitive as one might expect that enhanced photolytic destruction on planets around active M-dwarfs should suppress day-to-nightside contrasts. However, simulations forced by active SEDs have more isothermal atmospheres (i.e., weaker temperature inversions; Figure 3(a)), which promote vertical mixing of surface gases above the tropopause, contributing to higher r_{diff} values.

3.3. Effects of Surface Fluxes on Atmospheric Distribution: Case of Dimethyl Sulfide

On tidally locked planets, phototrophs are unlikely to emit biogenic gases globally (i.e., the assumption for all biosignature gases considered thus far); rather, photosynthetically derived emissions are likely to be restricted to the dayside. To see how a biosignature gas (e.g., DMS; C_2H_6S) may behave on a tidally locked planet, we conduct three experiments, each with a different DMS flux distribution assumption, i.e., Earth-like, tidally locked with global DMS flux, and tidally locked with dayside DMS flux (Figure 4). We find that global DMS emissions result in substantially lower r_{diff} values (∼0% and ∼43%; Figures 4(a)–(b)) compared to a strictly dayside DMS emission assumption (∼67%; Figure 4(c)). The larger value of r_{diff} in the latter simulation is due to the relatively short lifetime of DMS (Kloster et al. 2005).

Similar to the above DMS behavior, a potential consequence of tidal locking is the relegation of CH_4 and N_2O production to a single hemisphere, i.e., processes of methanogenesis and denitrification favor anaerobic conditions and may be disfavored on photosynthetic oxygen-producing daysides. Spatially variable surface to atmosphere flux distributions of CH_4 and N_2O therefore could exhibit higher r_{diff} than the values predicted here ($\lesssim$10%; Figures 1(e)–(f) and (h)-(i)).

4. Discussion

Here we discuss possible areas of future advancement, as well as the observational relevance of this study.

In this CCM study, we find that factors that determine biosignature concentration and distribution on a habitable tidally locked planet are species dependent. For example, ozone mixing ratios are primarily driven by photolytic production and destruction, while ozone distribution and nightside sustenance are controlled by its transport and lifetime. An additional consideration, here demonstrated in our DMS simulations, is the spatial variance of gas fluxes. Given that habitable exoplanets are likely to possess heterogeneous ecologies, whose fluxes will interface with attendant atmospheric structure and circulation patterns, spatially heterogeneous surface fluxes could have observationally distinguishable effects on atmospheric spectra. For example, dayside upwelling could facilitate vertical mixing of surface gases into the upper atmosphere (Figures 1(e)–(f)), while nightside radiation inversions could trap constituents near the surface, limiting vertical mixing, day–nightside interactions, and potentially observability. These scenarios, in which atmospheric dynamics, photochemistry, surface flux sources, and feedback processes play important roles highlight the utility of 3D CCM simulations. However, due to nonlinear interactions and internal atmospheric variability, disentangling drivers of emergent behavior is challenging and will likely require the tools of modern atmospheric and computational science, including Lagrangian tracking of constituents (e.g., Sölch & Kärcher 2010), single- and multimodel ensembles (e.g., Kay et al. 2015), and statistical analyses focused on detection and attribution (e.g., Horton et al. 2015; Diffenbaugh et al. 2017).

Despite these challenges, the introduction of 3D CCMs to exoplanet biosignature prediction efforts offers substantial research potential. Future applications are likely to consider a wider variety of Earth-like biospheres, e.g., markedly disparate atmospheres of Earth throughout geologic time (Arney et al. 2016; Rugheimer & Kaltenegger 2018), and should be expanded to include biologically constrained models and modules (Catling et al. 2018; Walker et al. 2018). Such applications will facilitate egocentricity avoidance—a commonly acknowledged goal of the field (e.g., Seager et al. 2013). Until then, use of default Earth conditions may restrict the relevance of 3D CCM findings to truly Earth-like planets, with similar atmospheric formation histories, ecospheres, and biological signatures resulting from oxygenic photosynthesis (Meadows et al. 2018b).

This study demonstrates that fully coupled CCMs are particularly promising for studies that seek to assess the roles of and feedbacks between different stellar SEDs, biological behaviors, and atmospheric compositions. Such efforts are consistent with recent reviews, discussing aspirational goals and the future of exoplanet biosignature research (Catling et al. 2018; Walker et al. 2018). Extrasolar astrophysical radiation environments and/or atmospheric conditions may alter biological activity, as life is both photochemically and climatologically mediated. Living organisms are highly receptive toward UV emissions such that UV-B ($290 < \lambda < 320$ nm) photons hinder metabolism, photosynthesis, and thus biological production rates (Teramura et al. 1994). Moreover, due to different climate and redox conditions, for example, on anoxic Archean Earth (∼3.0 Ga), hydrocarbons and

organosulfur biosignatures (C_2H_6, CH_4, OCS, DMS etc.) could rise to more prominent abundances and hence may be conducive to remote detection (Haqq-Misra et al. 2008; Domagal-Goldman et al. 2011; Hu et al. 2012; Arney et al. 2016).

In terms of the potential observational implications of our simulations, our results agree with those of Segura et al. (2005), Rauer et al. (2011), and Rugheimer et al. (2015), i.e., rocky planets orbiting active and quiet M-dwarfs should have deeper absorption depths, particularly for ozone and secondary biosignatures such as methane and nitrous oxide (as seen in transit and emission spectra). This makes habitable zone planets orbiting M-dwarfs favorable targets. 3D predictions from our CCM simulations may be confirmed by remote observations. Phase curve analysis can potentially resolve 3D atmospheric structures of super-Earth and Earth-sized terrestrial planets (Stevenson et al. 2014; Kreidberg & Loeb 2016). For example, thick substellar clouds could appear characteristically for planets with specific spin-orbit resonances (Yang et al. 2013).

In terms of biosignature measurements on tidally locked planets, different longitudinal gradients of gaseous constituents may affect measurements of variation spectra (peak amplitude of the phase curves) extracted from thermal phase curves (Selsis et al. 2011). As variation spectral signals depend on amplitude-peaks in orbital light curves, there may be added anisotropy due to time-varying longitudinal gas distributions on tidally locked planets in each orbit (assuming null obliquity, as seen in Figure 1). Compared to nontidally locked fast rotators (with similar stellar UV activity and orbital period), we predict that more pronounced absorption signals may seen in variation spectrum on tidally locked planets, driven by greater difference between maximum and minimum phase amplitudes due to uneven hemispheric gas distributions. The emission spectrum at maximum phase (direct line of sight) should correspondingly see similar behavior, at least for a few IR-windows (e.g., between 3 and 9 μm; Selsis et al. 2011). For direct imaging, one possibility is that these features may be more prominent during certain orbital phases. Ozone observability, for example, may decrease during secondary eclipses as the dayside with reduced ozone abundance would be Earth-facing. Radiative transfer models, using our CCM results as inputs, will be needed to quantitatively assess observational prospects of the above.

5. Conclusions

This Letter reports numerical simulations using a coupled 3D CCM to explore global distribution of biosignature gases on Earth-like and tidally locked planets as a function of stellar spectral type, stellar activity, and planetary rotation period. Qualitatively similar to 1D models, we find increased mixing ratios of biogenic compounds (e.g., O_3, CH_4, and N_2O) for both active and inactive M-dwarf SEDs. These increases are most pronounced for planets around quiet M-dwarfs. Even though the effects of tidal locking are noticeable in our simulations, they are not yet discernable with current observational techniques, i.e., the primary biosignatures simulated in this work (O_3, CH_4, N_2O) show low ($\lesssim$20%) day-to-nightside mixing ratio contrasts. Conversely, simulated day-to-nightside differences of photosynthetic compounds (e.g., DMS) are found to be nearly 70% and underscore the need for heterogeneous 3D realism in modeling biosignatures and their photochemical derivatives. Overall, this study serves as a stepping stone for future applications using 3D CCMs to study the habitability and spectral observability of terrestrial exoplanets.

H.C. thanks J. Schnell and A. Loeb for helpful discussions, as well as P. Paschos for assistance in the installation of CESM. E.T.W. thanks NASA Habitable Worlds grant 80NSSC17K0257 for support. Goddard affiliates are thankful for support from GSFC Sellers Exoplanet Environments Collaboration (SEEC), which is funded by the NASA Planetary Science Divisions Internal Scientist Funding Mode. The VPL team at the University of Washington is thanked for the stellar spectra data. Computational, storage, and staff resources were provided by the QUEST high performance computing facility at Northwestern University, which is jointly supported by the Office of the Provost, Office for Research, and Northwestern University Information Technology.

ORCID iDs

Howard Chen https://orcid.org/0000-0003-1995-1351
Eric T. Wolf https://orcid.org/0000-0002-7188-1648
Ravi Kopparapu https://orcid.org/0000-0002-5893-2471
Shawn Domagal-Goldman https://orcid.org/0000-0003-0354-9325
Daniel E. Horton https://orcid.org/0000-0002-2065-4517

References

Anglada-Escudé, G., Amado, P. J., Barnes, J., et al. 2016, Natur, 536, 437
Arney, G., Domagal-Goldman, S. D., Meadows, V. S., et al. 2016, AsBio, 16, 873
Barclay, T., Pepper, J., & Quintana, E. V. 2018, arXiv:1804.05050
Batalha, N. E., Lewis, N. K., Line, M. R., Valenti, J., & Stevenson, K. 2018, ApJL, 856, L34
Bolcar, M. R., Feinberg, L., France, K., et al. 2016, Proc. SPIE, 9904, 99040J
Burrows, A. S. 2014, PNAS, 111, 12601
Catling, D. C., Krissansen-Totton, J., Kiang, N. Y., et al. 2018, AsBio, 18, 709
Danabasoglu, G., & Gent, P. R. 2009, JCli, 22, 2494
Des Marais, D. J., Harwit, M. O., Jucks, K. W., et al. 2002, AsBio, 2, 153
Diffenbaugh, N. S., Singh, D., Mankin, J. S., et al. 2017, PNAS, 114, 4881
Domagal-Goldman, S. D., Meadows, V. S., Claire, M. W., & Kasting, J. F. 2011, AsBio, 11, 419
Dressing, C. D., & Charbonneau, D. 2015, ApJ, 807, 45
Fujii, Y., Del Genio, A. D., & Amundsen, D. S. 2017, ApJ, 848, 100
Gillon, M., Triaud, A. H. M. J., Demory, B.-O., et al. 2017, Natur, 542, 456
Greene, T. P., Line, M. R., Montero, C., et al. 2016, ApJ, 817, 17
Haqq-Misra, J., Wolf, E. T., Joshi, M., Zhang, X., & Kopparapu, R. K. 2018, ApJ, 852, 67
Haqq-Misra, J. D., Domagal-Goldman, S. D., Kasting, P. J., & Kasting, J. F. 2008, AsBio, 8, 1127
Henry, T. J., Jao, W.-C., Subasavage, J. P., et al. 2006, AJ, 132, 2360
Horton, D. E., Johnson, N. C., Singh, D., et al. 2015, Natur, 522, 465
Hu, R., Seager, S., & Bains, W. 2012, ApJ, 761, 166
Jacob, D. 1999, Introduction to Atmospheric Chemistry (Princeton, NJ: Princeton Univ. Press)
Kasting, J. F., Chen, H., & Kopparapu, R. K. 2015, ApJL, 813, L3
Kasting, J. F., Pollack, J. B., & Crisp, D. 1984, JAtC, 1, 403
Kay, J., Deser, C., Phillips, A., et al. 2015, BAMS, 96, 1333
Kettle, A., & Andreae, M. 2000, JGRD, 105, 26793
Kloster, S., Feichter, J., Maier-Reimer, E., et al. 2005, BGD, 2, 1067
Koll, D. D. B., & Abbot, D. S. 2016, ApJ, 825, 99
Kopparapu, R. k., Wolf, E. T., Arney, G., et al. 2017, ApJ, 845, 5
Kopparapu, R. k., Wolf, E. T., Haqq-Misra, J., et al. 2016, ApJ, 819, 84
Kreidberg, L., & Loeb, A. 2016, ApJL, 832, L12
Lamarque, J.-F., Emmons, L. K., Hess, P. G., et al. 2012, GMD, 5, 369
Lean, J., Beer, J., & Bradley, R. 1995, GeoRL, 22, 3195
Lewis, N. T., Lambert, F. H., Boutle, I. A., et al. 2018, ApJ, 854, 171
Lovelock, J. E. 1975, RSPSB, 189, 167
MacFarling Meure, C., Etheridge, D., Trudinger, C., et al. 2006, GeoRL, 33, 14
Mann, A. W., Feiden, G. A., Gaidos, E., Boyajian, T., & von Braun, K. 2015, ApJ, 804, 64

Meadows, V. S., Arney, G. N., Schwieterman, E. W., et al. 2018a, AsBio, 18, 133
Meadows, V. S., Reinhard, C. T., Arney, G. N., et al. 2018b, AsBio, 18, 630
Mennesson, B., Gaudi, S., Seager, S., et al. 2016, Proc. SPIE, 9904, 99040L
Neale, R. B., Chen, C.-C., Gettelman, A., et al. 2010, NCAR Technical Note, 1, 1
Proedrou, E., & Hocke, K. 2016, EP&S, 68, 96
Rauer, H., Gebauer, S., Paris, P. V., et al. 2011, A&A, 529, A8
Rugheimer, S., & Kaltenegger, L. 2018, ApJ, 854, 19
Rugheimer, S., Kaltenegger, L., Segura, A., Linsky, J., & Mohanty, S. 2015, ApJ, 809, 57
Sagan, C., Thompson, W. R., Carlson, R., Gurnett, D., & Hord, C. 1993, Natur, 365, 715
Schwieterman, E. W., Kiang, N. Y., Parenteau, M. N., et al. 2018, AsBio, 18, 663
Seager, S., Bains, W., & Hu, R. 2013, ApJ, 775, 104
Seager, S., Deming, D., & Valenti, J. A. 2009, ASSP, 10, 123
Segura, A., Kasting, J. F., Meadows, V., et al. 2005, AsBio, 5, 706
Seinfeld, J. H., & Pandis, S. N. 2012, Atmospheric Chemistry and Physics: from Air Pollution to Climate Change (New York: Wiley)
Selsis, F., Wordsworth, R. D., & Forget, F. 2011, A&A, 532, A1
Shields, A. L., Bitz, C. M., Meadows, V. S., Joshi, M. M., & Robinson, T. D. 2014, ApJL, 785, L9
Sölch, I., & Kärcher, B. 2010, QJRMS, 136, 2074
Stevenson, K. B., Désert, J.-M., Line, M. R., et al. 2014, Sci, 346, 838
Tarter, J. C., Backus, P. R., Mancinelli, R. L., et al. 2007, AsBio, 7, 30
Taylor, K. E., Stouffer, R. J., & Meehl, G. A. 2012, BAMS, 93, 485
Teramura, A. H., & Sullivan, J. H. 1994, Photosynthesis Research, 39, 463
Thompson, S. E., Coughlin, J. L., Hoffman, K., et al. 2018, ApJS, 235, 38
Wakeford, H. R., Sing, D. K., Kataria, T., et al. 2017, Sci, 356, 628
Walker, S. I., Bains, W., Cronin, L., et al. 2018, AsBio, 18, 779
Way, M. J., Del Genio, A. D., Kiang, N. Y., et al. 2016, GeoRL, 43, 8376
Wolf, E. T. 2017, ApJL, 839, L1
Wolf, E. T., & Toon, O. B. 2015, JGRD, 120, 5775
Wordsworth, R. 2015, ApJ, 806, 180
Yang, J., Cowan, N. B., & Abbot, D. S. 2013, ApJL, 771, L45
Yang, J., Leconte, J., Wolf, E. T., et al. 2016, ApJ, 826, 222